

Modelling the inelastic scattering of fast electrons

L.J. Allen ^{a,*}, A.J. D'Alfonso ^{a,1}, S.D. Findlay ^b

^a School of Physics, University of Melbourne, Parkville, Victoria 3010, Australia

^b School of Physics, Monash University, Clayton, Victoria 3800, Australia



ARTICLE INFO

Article history:

Received 28 July 2014

Received in revised form

10 October 2014

Accepted 13 October 2014

Available online 29 October 2014

Keywords:

Atomic resolution imaging

Inelastic scattering of fast electrons

Mixed dynamic form factor

ABSTRACT

Imaging at atomic resolution based on the inelastic scattering of electrons has become firmly established in the last three decades. Harald Rose pioneered much of the early theoretical work on this topic, in particular emphasising the role of phase and the importance of a mixed dynamic form factor. In this paper we review how the modelling of inelastic scattering has subsequently developed and how numerical implementation has been achieved. A software package μ STEM is introduced, capable of simulating various imaging modes based on inelastic scattering in both scanning and conventional transmission electron microscopy.

© 2014 Elsevier B.V. All rights reserved.

1. Introduction

A landmark paper entitled “Theory of image formation by inelastically scattered electrons in the electron microscope” was published 30 years ago by Helmut Kohl and Harald Rose [1]. There they observed that “reviews on image formation treat the contribution of inelastically scattered electrons as a deleterious side effect” but suggested that “it seems worthwhile to examine image formation by inelastically scattered electrons in more detail”. This insight spurred the subsequent development of high resolution spectroscopic imaging modes [2–5], but it would be fifteen years before the spectroscopic single atom imaging envisaged by Kohl and Rose was realised [6], and longer before atomic resolution spectroscopic imaging really came into its own [7–18].

In their seminal paper, Kohl and Rose [1] outline a quantum mechanical theory of imaging which considers both elastically and inelastically scattered electrons. Early on in their paper they address the importance of quantum mechanical phase in electron scattering and show how the concept of phase is related to a four-dimensional mixed dynamic form factor [19] encapsulating the essential physics of inelastic scattering. Kohl and Rose presented a clear conceptual picture to show that accounting for phase is essential, which we think worth repeating here. Consider the inelastic signal from an atom illuminated by an electron probe consisting of the coherent superposition of two plane waves with different incident angles, as shown in Fig. 1. A purely kinematic analysis might focus on the

scattering angles between each of these plane waves and the detector. However, the relative phase of the two waves is critical in determining where the electron density in their interference pattern sits relative to the atom position, something physical intuition correctly identifies as being essential in determining the resultant signal. In essence, the mixed dynamic form factor describes the contribution to the signal due to the interference between pairs of plane waves (Fourier components) in the probe. Though less obvious, it turns out that knowing the contribution from each pair of plane wave components is sufficient to determine the total contribution from an arbitrarily shaped incident wave field. This is important in scanning transmission electron microscopy where the incident convergent probe contains a multitude of different plane wave components [20,21].

Rose and co-workers generalised the work in Ref. [1] in terms of a mutual coherence function to also encapsulate incoherence in the probe electrons, in particular temporal incoherence [22]. They elucidated the basic governing equation for the mutual coherence function and discussed its solution via a generalised multislice formulation based on four dimensional propagators. Though the mutual coherence formalism has been used to gain conceptual insight into coherence in inelastic scattering (e.g. [23]), such an approach, involving four dimensional Fourier transforms, is demanding of computational resources – both in terms of memory and processing power. As we shall see in what follows, much of the intervening development has focused on ways of making calculations sufficiently tractable so that they may routinely be used to analyze experimental images.

Fundamental aspects of inelastic scattering in solids were addressed over a bit more than a decade, starting in the first half of the 1980s, by several authors [24–37]. In particular, Dudarev et al.

* Corresponding author.

E-mail addresses: lj@unimelb.edu.au (L.J. Allen), a.j.dalfonso.com.au (A.J. D'Alfonso).

¹ μ STEM enquiries.

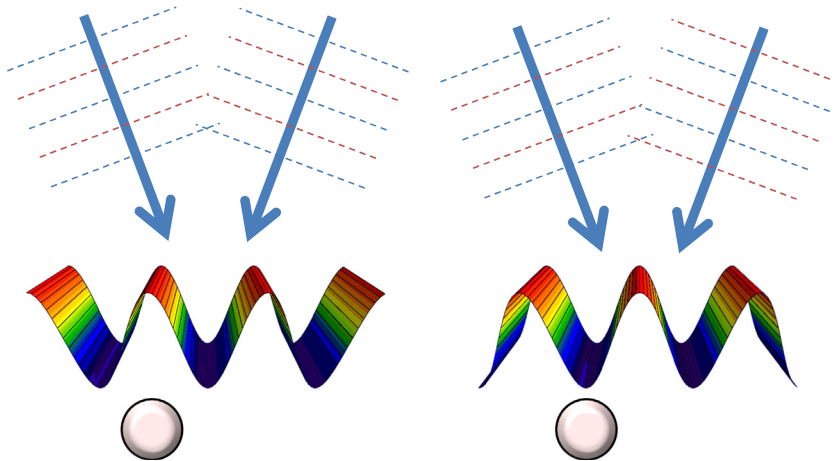


Fig. 1. Schematic showing how the relative phase of incident plane waves affects the electron density in the vicinity of an atom.

proceeded on the basis of a one particle density matrix, related to the mixed dynamic form factor, and its accompanying governing equation, the so-called kinetic equation [36]. Building on some of the earlier work, Allen and Josefsson presented a comprehensive theory of inelastic scattering, implicitly incorporating the mixed dynamic form factor, in a formulation based on Bloch waves [37]. The physical significance of the mixed dynamic form factor and its relation to the density matrix was comprehensively investigated by Schattschneider and co-workers [38,39]. How the mixed dynamic form factor arises and its role in inelastic scattering will be discussed in Section 2.

2. The mixed dynamic form factor

In this section we will show how the mixed dynamic form factor arises. Let us take as our starting point the following equation describing an inelastic scattering event that occurs at a specific depth z_i into the specimen [40,41], measured from the entrance surface of the specimen and along the optical axis:

$$\psi_n(\mathbf{P}, \mathbf{r}, z_i) = -i\sigma_n H_{n0}(\mathbf{r}, z_i)\psi_0(\mathbf{P}, \mathbf{r}, z_i). \quad (1)$$

The probe wave function ψ_0 at the depth z_i depends on the co-ordinate \mathbf{r} in a plane perpendicular to the optical axis. The functional dependence denoted by \mathbf{P} could be the tilt in conventional transmission electron microscopy, specified by the tangential component of the wave vector of the incident electrons \mathbf{k}_{0t} or, in scanning transmission electron microscopy, it might specify the probe position \mathbf{R} on the surface of the specimen. For notational simplicity, we will not show the parametric probe dependence \mathbf{P} explicitly everywhere in what follows, reintroducing it only when we reach key results. The projected inelastic transition potential H_{n0} describes an inelastic transition, via a Coulomb interaction, at the depth z_i from an initial state of the specimen labelled 0 to a final state labelled n , and its modulus squared gives the probability that transition will occur [41]. Here $\sigma_n = m/2\pi\hbar^2 k_n$ is the interaction constant for the fast electron after energy loss, in which m is the relativistic mass of the electron and k_n is the wave number of the fast electron after the inelastic transition. In summary, Eq. (1) shows that ψ_n , the inelastic wave function for the fast electron after the excitation, is proportional to the product of H_{n0} and ψ_0 .

It is worth emphasising at this point that ψ_n would only be physically observed in isolation if we had a simultaneous, independent measurement showing that the specimen final state n was realised. Since this is almost never the case, the rules of quantum mechanics dictate that we must sum over all final states consistent with the quantities measured. This leads to the density matrix formulation. Some may therefore object to the use of the

term “wave function” to describe ψ_n since it seems to suggest a physical reality to the quantity, whereas an infinite number of different final state bases $\{\psi_n\}$ may be used to generate the density matrix, which is related to what is physically measured [42]. However, the ψ_n are valid building blocks from which to construct the density matrix if desired. Moreover, this approach can be made efficient via considered selection of the specimen basis states [41], and we will persist in using the term “wave function” to describe them.

In three dimensions the transition potentials have the form

$$H_{n0}(\mathbf{x}) = \frac{e^2}{4\pi\epsilon_0} \int u_f^*(\mathbf{x}') \frac{1}{|\mathbf{x} - \mathbf{x}'|} u_i(\mathbf{x}') d\mathbf{x}', \quad (2)$$

where $u_i(\mathbf{x})$ and $u_f(\mathbf{x})$ represent initial and final state wave functions in three dimensions. The prefactor contains the magnitude of the charge on an electron e and the permittivity of free space ϵ_0 . The assumption here is that the inelastic transition effectively occurs in vacuum but this can be generalised, if needed, by incorporating a suitable dielectric function in Eq. (2). The projected transition potentials $H_{n0}(\mathbf{r}, z_i)$ in Eq. (1) are obtained as follows [40,41,43]:

$$H_{n0}(\mathbf{r}, z_i) = \int H_{n0}(\mathbf{x}) e^{2\pi i(k_0 - k_n)z} dz, \quad (3)$$

where k_0 is the wave number of the incident electron before the inelastic scattering event. Eq. (3) implicitly assumes that the inelastic transition is localised to a particular depth z_i in the crystal. This is generally agreed to be a reasonable assumption for inner-shell ionisation by fast electrons because the core electrons are so tightly bound [27,28]. In such cases, the range of the z integration along the optical axis about the depth z_i need only extend over a finite range where the integrand is significantly different from zero. The more general case introduces many subtleties [44] and will not be considered here.

Examples of selected projected transition potentials, as introduced in Eqs. (1) and (3), are shown in Fig. 2 for the $L_{2,3}$ ionisation edge in Si. In particular, note the differing localisations of the dipole and quadrupole transitions in Fig. 2(a) and (b) respectively. An asymmetric quadrupole transition is shown in Fig. 2(c) and (d). An appreciation and understanding of the scale and extent of these potentials relative to the illuminating, elastically scattered wave is necessary to correctly interpret inelastic images based on inner-shell ionisation. The transition potentials are calculated in an angular momentum basis and details may be found in Ref. [45].

We now elucidate how an inelastic wave is generated for a 100 keV plane wave incident on a specimen of Si_3N_4 . Fig. 3 shows the probability density for an electron which undergoes inelastic

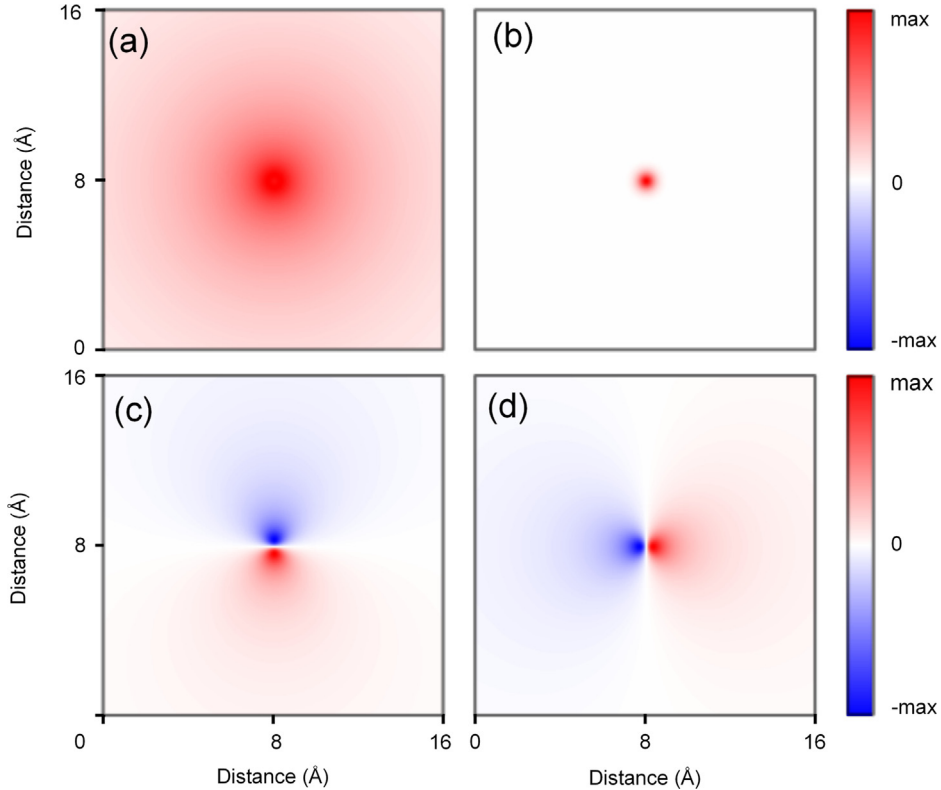


Fig. 2. Selected projected transition potentials for ionisation of the $L_{2,3}$ edge in Si (1 eV above the edge) using an angular momentum basis and 100 keV incident electrons. The initial and final states for the plotted transitions are $(l, m_l) = (1, 0)$ and (a) $(l', m'_l) = (0, 0)$, a dipole allowed transition and purely imaginary; (b) $(l', m'_l) = (3, 0)$, a quadrupole allowed transition and purely real; and the (c) real and (d) imaginary components of $(l', m'_l) = (3, 1)$, a quadrupole allowed transition. Each transition potential is on its own scale: (a) -0.09 to $+0.09 \text{ \AA eV}^{1/2}$, (b) -0.07 to $+0.07 \text{ \AA eV}^{1/2}$ and (c) and (d) -0.87 to $+0.87 \text{ \AA eV}^{1/2}$.

scattering within a specimen of Si_3N_4 oriented along the [0001] zone axis, for a range of depths. The inelastic transition takes place in the column of Si atoms indicated by the white (larger) arrow on the projected potential (a thermally smeared potential for elastic scattering) displayed in the panel on the bottom, right-hand side of Fig. 3 and at a depth of approximately 61 Å (21 unit cells into the specimen). We assume ionisation of a Si $L_{2,3}$ electron in the Si atom, specifically via the $(l=1, m_l=0) \rightarrow (l'=0, m'_l=0)$ dipole transition. The transition potential for this transition (which is pure imaginary) is shown in the panel to the left of the projected potential for elastic scattering. Elastic channelling of the probe up to 61 Å is illustrated in the first two and a half rows in Fig. 3. After ionisation (see the green box) the wave function describing the electron, with wave vector reduced according to the energy loss, has probability density localised around the atom which has been ionised and is, to a rough first approximation, an outgoing spherical wave emanating from the column of Si atoms. However, probability density is evident on surrounding columns, even immediately after the ionisation event. This is due to the delocalised nature of this particular inelastic transition. There is considerable overlap between H_{n0} and ψ_0 in Eq. (1) and in the vicinity of the ionisation event some features of the elastic contrast are preserved. This is an example of a partial preservation of elastic contrast. (For more delocalised inelastic interactions, a larger amount of elastic contrast can be preserved [46]). Channelling of the inelastically scattered electron then occurs as it propagates to the exit surface, with increasing probability density on the adjacent N column, indicated on the bottom right of Fig. 3 by the cyan (smaller) arrow, clearly evident.

Now consider rather a focused scanning probe situated above a column of N atoms the specimen of Si_3N_4 , the column indicated by cyan (smaller) arrow in the panel on the bottom, right-hand

side of Fig. 4, where once again a thermally smeared, projected potential for elastic scattering is displayed. The probe parameters are given in the figure caption. Initially the probe is focused on the N column and cross talk with the adjacent Si column, indicated by the white (larger) arrow, becomes evident in the first two and a half rows of the figure. Ionisation of a $L_{2,3}$ electron in a Si atom in the adjacent column occurs at a depth of 61 Å, once again via the $(l=1, m_l=0) \rightarrow (l'=0, m'_l=0)$ dipole transition. As a result of the inelastic interaction we see that the intensity on the Si column becomes larger than that on the N column. However, due to the long range nature of the dipole transition probability, as can be seen in the panel second from the right at the bottom of Fig. 4, the overlap with the probe is such that substantial intensity remains on the N column. Once again, there has been a degree of preservation of elastic contrast. The probability density then evolves slowly as one propagates towards the exit surface of the specimen.

After an inelastic transition has occurred, the wave function of the fast electron can be considered to be one of the final states in the set $\{\psi_n\}$. Not only is the energy of the fast electron probe reduced by the inelastic scattering, but, since the transition potential $H_{n0}(\mathbf{r}, z_i)$ is complex, the amplitude and phase of the wave function also changes. The important point to note is that the inelastic wave has a well defined phase. Fourier transforming Eq. (1) we obtain

$$\Psi_n(\mathbf{q}, z_i) = -i\sigma_n \int H_{n0}(\mathbf{r}, z_i) \psi_0(\mathbf{r}, z_i) e^{-2\pi i \mathbf{q} \cdot \mathbf{r}} d\mathbf{r}. \quad (4)$$

A density matrix can be defined in \mathbf{q} space by

$$\sum_n \Psi_n^*(\mathbf{q}, z_i) \Psi_n(\mathbf{q}', z_i). \quad (5)$$

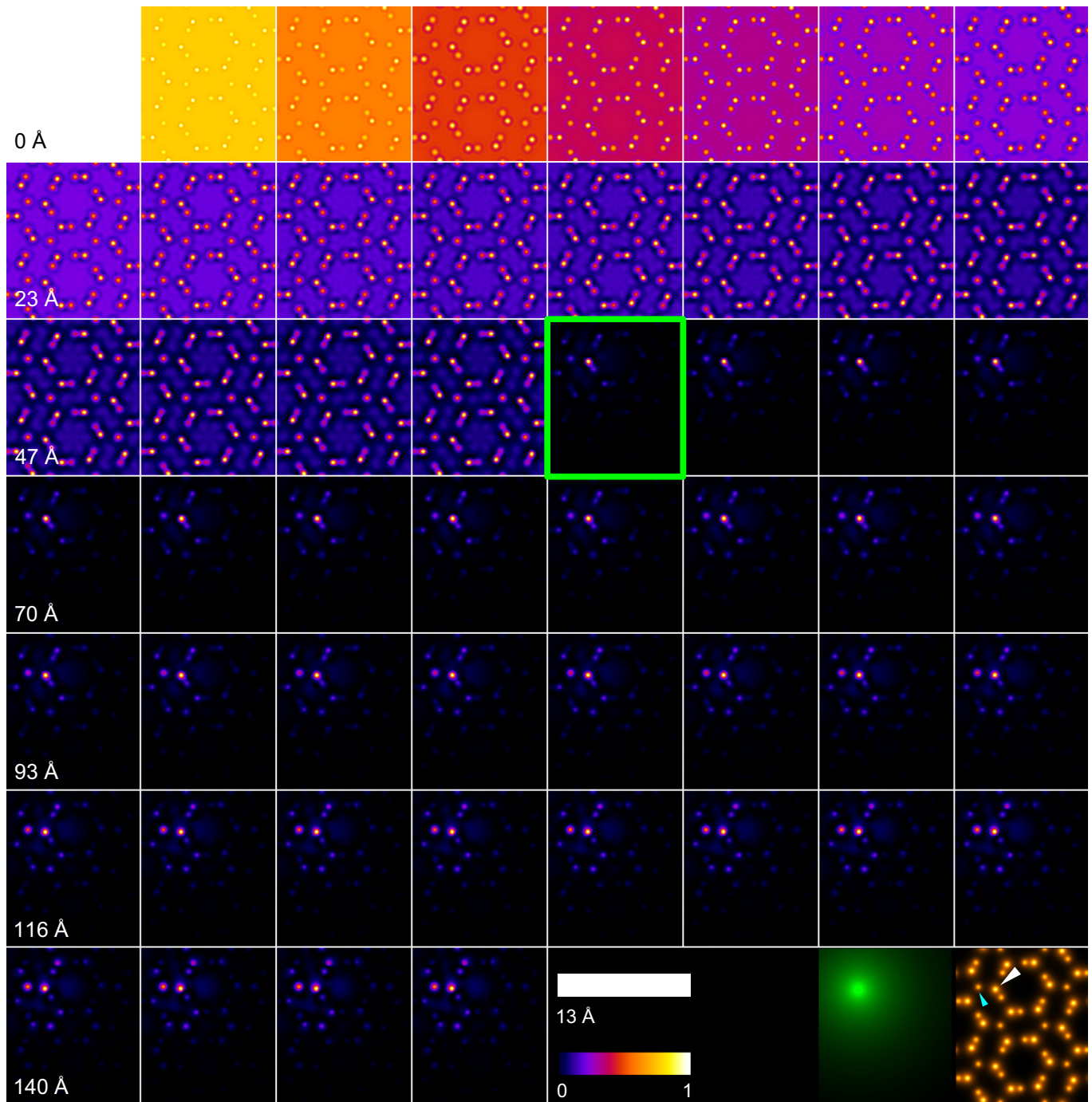


Fig. 3. Electron probability density of the probing electron within a specimen of Si_3N_4 , along the [0001] zone axis, in the conventional transmission electron microscopy geometry (plane wave incidence). The depth within the specimen increases in steps of 2.9 \AA , moving from left to right. Each image is scaled between zero and unity. A 100 kV accelerating voltage is assumed. The position of columns of Si and N atoms is indicated by the brighter (larger) circles and of the columns of N atoms by the dimmer (smaller) circles in the projected potential shown on the bottom right of the figure. An $(l=1, m_l=0) \rightarrow (l'=0, m'_l=0)$ transition, 1 eV above the Si $L_{2,3}$ ionisation edge (transition potential second panel from right, bottom) occurs at a depth of 61 \AA (green box) in the column indicated by the white (larger) arrow on the bottom right panel. The N column indicated by the cyan (smaller) arrow is referred to in the text. (For interpretation of the references to color in this figure caption, the reader is referred to the web version of this article.)

Consider the case of energy-filtered transmission electron microscopy [47,48]. The density matrix in Eq. (5) may now be propagated in 4D (which involves the use of 4D Fourier transforms) to the exit surface of the specimen and then through the lens using a 4D lens transfer function. The diagonal elements of the resulting density matrix in real space provide the energy filtered image. Alternatively, one can propagate each of the wave functions in Eq. (5) separately to the exit surface (which involves 2D Fourier transforms), apply a 2D lens transfer function and obtain the contribution from this final

state in the image plane. The contributions from all final states are then added incoherently. This yields the same image but is the preferred numerical procedure in terms of both memory and processing requirements.

Now let us discuss scanning transmission electron microscopy. There is no post specimen imaging lens; instead a detector (spectrometer) is positioned in the diffraction plane. We note that for a large enough acceptance angle on the detector, the subtleties due to the subsequent channelling of the inelastically scattered electron are

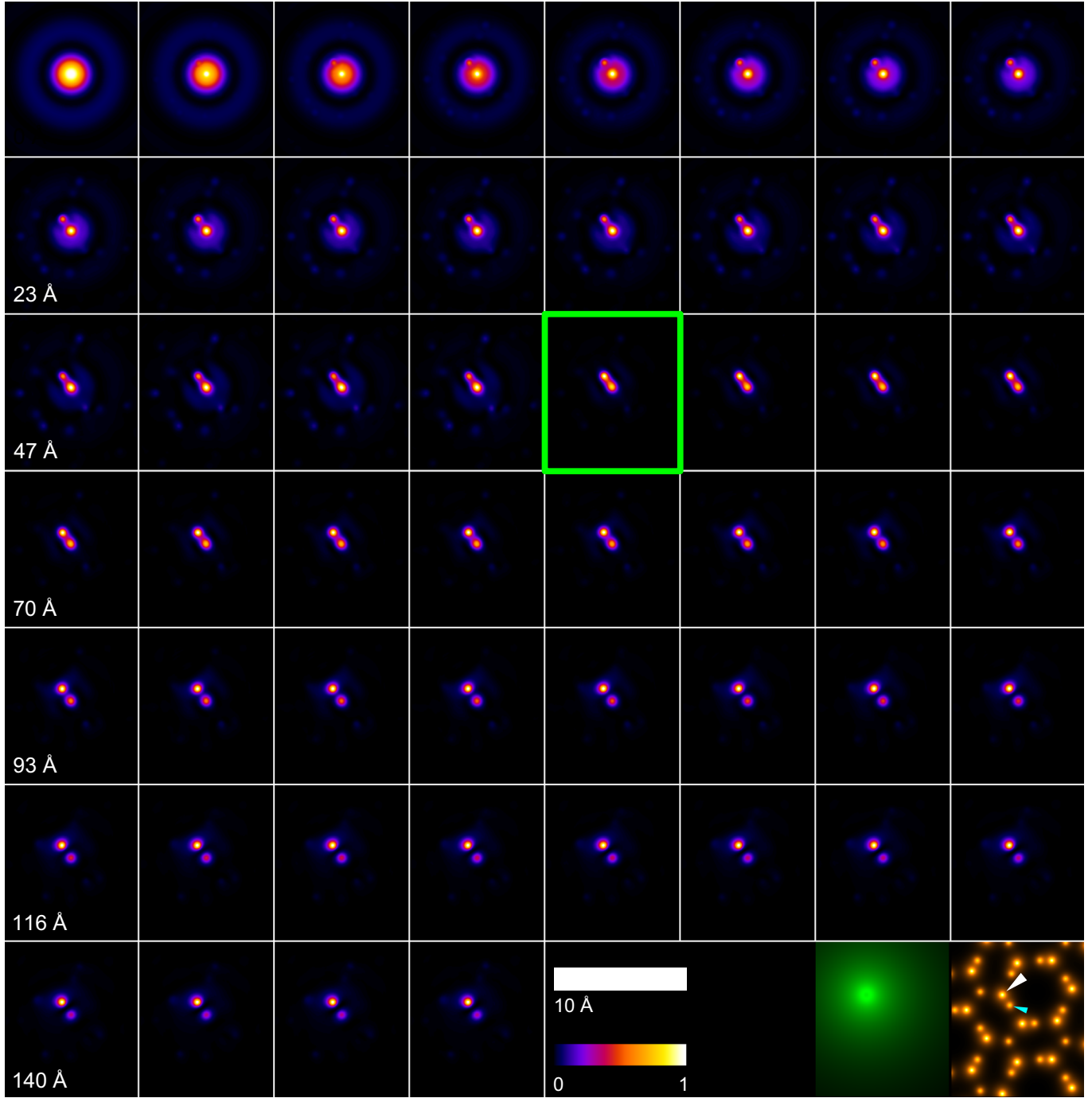


Fig. 4. Electron probability density of the probing electron within a specimen of Si_3N_4 , along the [0001] zone axis in the scanning transmission electron microscopy geometry (focused probe incidence). The depth within the specimen increases in steps of 2.9 \AA , moving from left to right. Each image is scaled between zero and unity. A 100 kV accelerating voltage is assumed. The position of columns of Si atoms is shown by the brighter (larger) circles and columns of N atoms by the dimmer (smaller) circles in the projected potential shown on the bottom right-hand side of the figure. The aberration-free probe is initially focused on the N column indicated in that panel by the cyan (smaller) arrow and is defined by a probe forming aperture of 25 mrad (0.68 \AA^{-1}). An $(l=1, m_l=0) \rightarrow (l'=0, m_l=0)$ transition, 1 eV above the $\text{Si } L_{2,3}$ ionisation edge (transition potential second panel from right, bottom) occurs at a depth of 61 \AA (green box) on the adjacent Si column indicated by the white (larger) arrow. (For interpretation of the references to color in this figure caption, the reader is referred to the web version of this article.)

integrated over [49,50] and a similar result can be obtained via a free space propagation to the detector. In that case the wave function in the diffraction (detector) plane is given directly by Eq. (4). The recorded signal is obtained by multiplying by a current conversion factor k_n/k_0 [36], taking into account the pertinent final states and integrating over the appropriate detector aperture D in the diffraction plane. This yields

$$I(z_i) = \int_D \sum_{n \neq 0} \frac{k_n}{k_0} |\Psi_n(\mathbf{q}, z_i)|^2 d\mathbf{q}$$

$$= \int_D \sum_{n \neq 0} \frac{k_n}{k_0} \sigma_n^2 \left| \int H_{n0}(\mathbf{r}, z_i) \psi_0(\mathbf{r}, z_i) e^{-2\pi i \mathbf{q} \cdot \mathbf{r}} d\mathbf{r} \right|^2 d\mathbf{q}, \quad (6)$$

where Eq. (1) has been used. Expanding the modulus squared and reordering the integrations yields

$$I(z_i) = \frac{2\pi}{h\nu} \iint \psi_0^*(\mathbf{r}, z_i) W(\mathbf{r}, \mathbf{r}', z_i) \psi_0(\mathbf{r}', z_i) d\mathbf{r} d\mathbf{r}', \quad (7)$$

where

$$W(\mathbf{r}, \mathbf{r}', z_i) = \frac{2\pi m}{h^2} \sum_{n \neq 0} \frac{1}{k_n} H_{n0}^*(\mathbf{r}, z_i) H_{n0}(\mathbf{r}', z_i) \int_D e^{2\pi i \mathbf{q} \cdot (\mathbf{r} - \mathbf{r}')} d\mathbf{q} \quad (8)$$

and $v = \hbar k_0/m$.

The total signal from inelastic transitions at different depths z_i is the incoherent sum

$$\begin{aligned} I(\mathbf{R}) &= \sum_i I(\mathbf{R}, z_i) \\ &= \frac{2\pi}{hv} \sum_i \iint \psi_0^*(\mathbf{R}, \mathbf{r}, z_i) W(\mathbf{r}, \mathbf{r}', z_i) \psi_0(\mathbf{R}, \mathbf{r}', z_i) d\mathbf{r} d\mathbf{r}'. \end{aligned} \quad (9)$$

where, since we are considering the case of a focused coherent probe, we have made the possible parametric probe dependence \mathbf{P} in Eq. (1) explicit as the probe position \mathbf{R} . Let us briefly consider what all this means for, say, the case of inner-shell ionisation of a particular edge in a particular atomic species in the specimen. In reality we consider a slice at depth z_i over which we must calculate the projected potentials $H_{n0}(\mathbf{r}, z_i)$ for all possible final states of the ejected electron for a range of energy losses for the fast electron and for all pertinent atoms in the slice [43]. Then we incoherently sum the contributions from all slices in the specimen. We note that, although the context in which Eq. (9) has been derived is that of a coherent focused probe, an equation of similar form is pertinent for the plane wave incidence of conventional transmission electron microscopy. In that case the dependence on probe position \mathbf{R} could be replaced by the tangential component of the wave vector of the incident electrons \mathbf{k}_{0t} (in many applications zero).

Eq. (9) makes it absolutely clear, through the presence of the $\psi_0(\mathbf{R}, \mathbf{r}', z_i)$ terms describing the probe in plane z_i inside the specimen, that the measured signal depends on how the probe wave function has scattered through the specimen. The dynamic evolution of the probe via elastic scattering can serve to redistribute electron probability density to columns other than that on which the probe is positioned [51], a possibility often referred to as “cross talk”. Eq. (9) also makes clear that both the amplitude and the phase of the probe wave field affect the measured intensity, the “effective scattering potential” $W(\mathbf{r}, \mathbf{r}', z_i)$ weighting the contribution of the relative-phase-dependent off-diagonal components of the density matrix $\psi_0^*(\mathbf{R}, \mathbf{r}, z_i) \psi_0(\mathbf{R}, \mathbf{r}', z_i)$. This is worth emphasising because, on the face of it, the first line in Eq. (6) does not depend on the phase of the wave functions. Further consideration, however, reveals that while the measurement does not depend on the phase of $\Psi_n(\mathbf{R}, \mathbf{q}, z_i)$ in reciprocal space, the distribution of the intensity in the diffraction plane, and in particular how much falls within as opposed to outside of the detector aperture D , is highly dependent on the real-space phase profile of $\psi_n(\mathbf{R}, \mathbf{r}, z_i)$.

Let us now make the link to the mixed dynamic form factor. We note that in Eq. (8) the transition potentials are separate from the detector geometry:

$$W(\mathbf{r}, \mathbf{r}', z_i) \equiv \tilde{W}(\mathbf{r}, \mathbf{r}', z_i) D(\mathbf{r} - \mathbf{r}'), \quad (10)$$

where

$$\tilde{W}(\mathbf{r}, \mathbf{r}', z_i) = \frac{2\pi m}{h^2} \sum_{n \neq 0} \frac{1}{k_n} H_{n0}^*(\mathbf{r}, z_i) H_{n0}(\mathbf{r}', z_i) \quad (11)$$

and

$$D(\mathbf{r} - \mathbf{r}') = \int_D e^{2\pi i \mathbf{q} \cdot (\mathbf{r} - \mathbf{r}')} d\mathbf{q}. \quad (12)$$

If we Fourier transform $\tilde{W}(\mathbf{r}, \mathbf{r}', z_i)$ given by Eq. (11) we obtain

$$\tilde{W}(\mathbf{g}, \mathbf{g}', z_i) = \frac{2\pi m}{h^2} \sum_{n \neq 0} \frac{1}{k_n} H_{n0}^*(\mathbf{g}, z_i) H_{n0}(\mathbf{g}', z_i), \quad (13)$$

where

$$H_{n0}(\mathbf{g}, z_i) = \int H_{n0}(\mathbf{r}, z_i) e^{-2\pi i \mathbf{g} \cdot \mathbf{r}} d\mathbf{r}. \quad (14)$$

Defining

$$F_{n0}(\mathbf{g}, z_i) = g^2 H_{n0}(\mathbf{g}, z_i) \quad (15)$$

and $\overline{k_n}$ as an average value for the set $\{k_n\}$ we may then write

$$\tilde{W}(\mathbf{g}, \mathbf{g}', z_i) \approx \frac{2\pi m}{h^2 \overline{k_n} g^2 g'^2} \sum_{n \neq 0} F_{n0}^*(\mathbf{g}, z_i) F_{n0}(\mathbf{g}', z_i), \quad (16)$$

which is an exact equality for a fixed energy loss and where the quantity

$$S(\mathbf{g}, \mathbf{g}', z_i) = \sum_{n \neq 0} F_{n0}^*(\mathbf{g}, z_i) F_{n0}(\mathbf{g}', z_i), \quad (17)$$

may be identified as a mixed dynamic form factor [1,38] and takes into account the interference (i.e. the relative phase) between $F_{n0}^*(\mathbf{g}, z_i)$ and $F_{n0}(\mathbf{g}', z_i)$.

Now let us return to Eq. (8). If the integration area D is sufficiently large then the exponential term effectively becomes a delta function, $\delta(\mathbf{r} - \mathbf{r}')$, and we may make the approximation

$$\begin{aligned} W(\mathbf{r}, \mathbf{r}', z_i) &\approx \frac{2\pi m}{h^2} \tilde{W}(\mathbf{r}, \mathbf{r}', z_i) \delta(\mathbf{r} - \mathbf{r}') \\ &= \frac{2\pi m}{h^2} \sum_{n \neq 0} \frac{1}{k_n} |H_{n0}(\mathbf{r}, z_i)|^2 \delta(\mathbf{r} - \mathbf{r}') \\ &\equiv 2V(\mathbf{r}, z_i) \delta(\mathbf{r} - \mathbf{r}'), \end{aligned} \quad (18)$$

where $\tilde{W}(\mathbf{r}, \mathbf{r}', z_i)$ are the diagonal terms in Eq. (11) (anticipating integration up over the delta function) and the factor of two in the last line has been inserted for consistency with the conventional definition of the local effective scattering potential $V(\mathbf{r}, z_i)$.

With the approximation in Eq. (18), Eq. (9) reduces to

$$\begin{aligned} I(\mathbf{R}) &= \sum_i I(\mathbf{R}, z_i) \\ &= \frac{4\pi}{hv} \sum_i \int_A |\psi_0(\mathbf{R}, \mathbf{r}, z_i)|^2 V(\mathbf{r}, z_i) d\mathbf{r}. \end{aligned} \quad (19)$$

This generic form has previously been derived by several authors, see for example Refs. [52,53,20]. The cross section is now effectively dependent only on the probe intensity at a point \mathbf{r} weighted by a local potential describing the inelastic scattering. Then only the diagonal terms $\psi_0^*(\mathbf{R}, \mathbf{r}, z_i) \psi_0(\mathbf{R}, \mathbf{r}, z_i) = |\psi_0(\mathbf{R}, \mathbf{r}, z_i)|^2$ of the density matrix contribute and the measurement is no longer sensitive to the relative phase of the probe at different spatial points. This is consistent with our discussion of the phase of the elastic wave field $\psi_0(\mathbf{R}, \mathbf{r}, z_i)$ affecting how much intensity in the diffraction plane falls inside and outside of the detector D : if the detector is sufficiently large then *all* the inelastic intensity for the class of inelastic interaction we are considering (for example all electrons that have lost an energy 10 eV above the edge after ionisation of a particular shell) falls inside the detector, and the phase of $\psi_0(\mathbf{R}, \mathbf{r}, z_i)$ ceases to affect the inelastic signal.

It is worth noting that even if we can make the local potential approximation in Eq. (18), if we take as our starting point the mixed dynamic form factor in Eq. (17), then that does not assume a diagonal form. The Fourier transform of the single-coordinate local effective scattering potential defined in Eq. (18) is a single-coordinate “effective scattering factor”. However, this is not the diagonal of the mixed dynamic form factor defined in Eq. (17).

3. Thermal diffuse scattering

A beam of fast electrons incident on a crystal produces a diffraction pattern which exhibits several well-known features including Bragg peaks, a diffuse background, higher-order-Laue-zone rings and

Kikuchi bands [54]. Phonon excitation (thermal scattering) makes an important contribution to many of these features, in particular the diffuse background and Kickuchi lines [55]. Thermal scattering also makes the essential contribution to high-angle annular dark field measurements in scanning transmission electron microscopy [56,57]. It also plays an important role in transmission electron microscopy [58] and convergent beam electron diffraction patterns [59,60].

In using Eq. (9) [or the special case given by Eq. (19)] to calculate an image due to inelastic scattering, say inner-shell ionisation, we need to know the probe wave function $\psi_0(\mathbf{r}, z_i)$ at various depths z_i in the specimen. Usually the values z_i would correspond to slices in a multislice formulation to solve the governing equation for the elastic wave function. However, inelastic scattering, and in particular thermal diffuse scattering due to the excitation of phonons, leads to loss of flux from the elastic channel. This can be taken into account using a local absorptive potential in the Schrödinger equation:

$$-\frac{\hbar^2}{2m}\nabla^2\psi_0(\mathbf{r}, z) + e[V_{\text{elas}}(\mathbf{r}, z) + iV(\mathbf{r}, z)]\psi_0(\mathbf{r}, z) = E\psi_0(\mathbf{r}, z), \quad (20)$$

where $V_{\text{elas}}(\mathbf{r}, z)$ is the potential for elastic scattering and the absorptive potential for thermal diffuse scattering $V(\mathbf{r}, z)$ is formally given in terms of transition potentials as in Eq. (18). Such an absorptive potential can also be calculated by other means as discussed by, for example, Refs. [31,55,61]. The absorptive potential approach is problematic in the sense that, once electrons are absorbed (have undergone thermal scattering), further (i.e. multiple) thermal scattering is not accounted for in the simulation. Furthermore, the contribution of thermally scattered electrons to other inelastic processes (for example ionisation) is not taken into account. The significance of multiple thermal scattering is illustrated in Fig. 5, which compares experimental high-angle annular dark field (or Z-contrast) images [62], Fig. 5(a), against two different simulation approaches, Fig. 5(b) and (c). Both experiment and simulation are on the same scale, and it is thus evident that the second simulation approach, Fig. 5(c), which is an absorptive calculation and thus neglects multiple thermal scattering, underestimates the number of electrons scattered into the annular detector. By contrast, good quantitative agreement with experiment is achieved by the first simulation approach, which does contain multiple thermal scattering. This first approach is the so-called frozen phonon model.

The frozen phonon model [59,60,63,64] incorporates multiple thermal scattering and also allows the contribution to other inelastic scattering events from thermally scattered electrons to be elucidated [65,66]. Elastic and thermal scattering is treated in a unified way, as in the later work of Dinges and Rose [67]. The frozen phonon model is a semi-classical approach based on the idea that the time taken for the fast electron to traverse the crystal is much faster than the oscillation period of an atom. Within this semi-classical model “the electron sees a snapshot of the atom frozen mid-vibration” [63]. The model assumes that each electron scatters elastically from a lattice of atoms frozen in position, the positions being drawn from a set of possibilities defined by statistical distribution functions which depend on the temperature factors for the atoms in the specimen. If an Einstein model is adopted and the crystal is modelled as a set of independent harmonic oscillators, then an atom has the following probability distribution for its position τ :

$$P(\tau) \propto \exp[-(\tau - \tau_0)^2 / 2\langle u^2 \rangle], \quad (21)$$

where τ_0 is the equilibrium position of the atom and $\langle u^2 \rangle$ is the mean-squared displacement of the atom. For many materials, experimental and simulated values for the mean-square displacement, or the closely related Debye–Waller factor, are available in the literature, see for example Refs. [68,69].

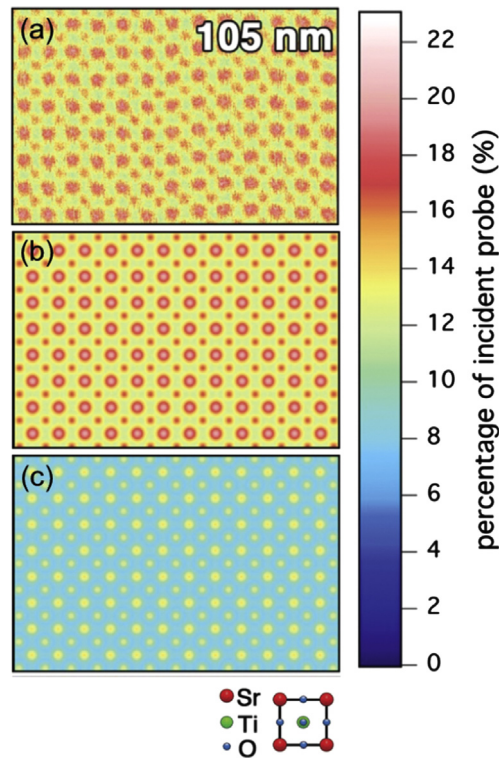


Fig. 5. (a) Experimental high-angle annular dark field images of a 105 nm thick specimen of SrTiO_3 along $\langle 100 \rangle$ with intensity variations normalised to the incident beam intensity (see color scale bar on the right). The strontium columns are the brightest and the titanium/oxygen columns are the second brightest features (see unit cell schematic). (b) Frozen phonon image simulations. (c) Absorptive model simulations (done in a Bloch wave model). Simulations have been convolved with a 0.08 nm FWHM Gaussian to take into account the finite source size. Adapted from Ref. [62].

The probability distributions for different electrons are summed incoherently in the detector plane. In practice this is implemented by a Monte Carlo integration. The frozen phonon model has produced simulations that compare well with experiment [62]. However, the frozen phonon model does not contain within its conceptual framework the momentum or energy transfer one would normally associate with inelastic scattering (in this case phonon excitation). Furthermore, from a quantum mechanical point of view one electron does not “see” a single possible configuration of the system, it “knows” about all possibilities.

There have been notable investigations into why the frozen phonon model nevertheless has been remarkably successful. Wang [70] carried out a term-by-term comparison in series expansion solutions of the frozen phonon model and the Yoshioka coupled channels equations (in density matrix form) [71]. More recently, Van Dyck [72] presented a simpler derivation of equivalence with a quantum mechanical approach by separating the “elastic” (in the frozen phonon model the “time” or configuration independent part) and inelastic scattering intensity. It was shown that each model predicted the diffracted intensity with an equation of the same mathematical form as the *single* inelastic scattering case.

A better model for thermal scattering based on many-body quantum mechanics, as expressed by the equations of Yoshioka [71], has been proposed by Forbes et al. [73]. In that approach phonon excitation is treated as a quantum excitation of the crystal during which the incident electron is inelastically scattered, losing energy of the order of mV, with all possible initial configurations of the system taken into account for that electron. We will refer to this approach as the quantum excitation of phonons model. If the same model for atomic displacements is used as in the frozen

phonon model then this approach yields the same electron probability density for a single electron in any plane as does the frozen phonon model for the electron probability density averaged over many incident electrons. Thus the frozen phonon model fortuitously yields a result which is operationally the same as that of the quantum excitation of phonons model for both elastically and thermally scattered electrons. However, besides being based on the correct quantum mechanics, an important feature of the quantum excitation of phonons model is that elastic and thermal scattering probabilities can be tracked separately at every stage of the calculation. In Fig. 6(a) we show the contribution for thermal scattering from strontium titanate in the diffraction plane.

4. Inner-shell ionisation

Two important modes of imaging are based upon the inelastic scattering associated with ionisation within the specimen. Elemental mapping in two dimensions at atomic resolution using electron energy-loss spectroscopy (EELS) based on inner-shell ionisation has evolved since it was demonstrated in 2007 [9–12,74] and is now at the point where it can be used to solve problems of technological interest [14]. However, unless the detector collection angle is very large, EELS is a partially coherent imaging mode – by which we mean, as per Eq. (9), it depends not only on the probe intensity distribution but also on its phase – and this may hinder simple interpretation of images. As an alternative to EELS one can use energy-dispersive x-ray (EDX) analysis, detecting the x-rays which are emitted subsequent to ionisation. EDX elemental mapping is an incoherent mode of imaging – by which we mean it is well described via Eq. (19) without recourse to the more general but complicated Eq. (9) – and image interpretation may therefore be simpler than for EELS. EDX imaging is thus more reminiscent of the widely used technique of high-angle annular dark field imaging, but with the advantage that elemental information is directly available for a range of different elements and x-ray peaks. A further advantage of EDX mapping relative to EELS is the accessibility of higher energy-loss peaks and their associated increased localisation. The first two-dimensional atomic resolution elemental maps based on EDX were published as recently as 2010 [15,16] and considerable improvements in the quality of such data have followed [17]. Quantification in EDX has recently been addressed [18].

Atomic resolution maps obtained in EELS are based on detecting electrons that have lost energy on transiting through the specimen due to inelastic scattering and which are scattered into a range of angles in the forward direction, defined by the collection aperture of the spectrometer. We then consider the integrated signal from a subset of those electrons falling into a suitable energy-loss window above the threshold energy for a particular core-loss edge. In the EDX imaging mode, when detecting x-rays associated with a particular edge, all possible kinematics of the inelastically scattered fast electron are effectively sampled since there is no restriction to scattering in the forward direction imposed by the EELS spectrometer. In addition, the energy window effectively extends over all possible energies above the threshold. So we expect that EELS with a large detector aperture and a large energy window, starting at threshold, would have similar underlying physics to EDX-based elemental mapping.

Allen and collaborators have shown how to calculate, in tandem with the frozen phonon model, the contribution to the combined ionisation signal from the elastic and (multiple) thermal diffuse scattering [65], with a similar approach being presented in Ref. [75]. In essence one uses Eq. (9) repeatedly for an adequate sampling of different frozen phonon configurations set up using Eq. (21) and sums the signal from each configuration incoherently. In calculating an inelastic signal in the quantum excitation of phonons model we

include the same sum over possible initial states of the system, but now for a single electron. To express this we can write Eq. (9) in the more general form

$$I(\mathbf{R}) = \frac{2\pi}{h\nu} \sum_{j,i} \int \int \psi_{0,j}^*(\mathbf{R}, \mathbf{r}, z_i) W_j(\mathbf{r}, \mathbf{r}', z_i) \psi_{0,j}(\mathbf{R}, \mathbf{r}', z_i) d\mathbf{r} d\mathbf{r}', \quad (22)$$

the implication being that the functions $\psi_0(\mathbf{R}, \mathbf{r}, z_i)$ in Eq. (9) are calculated for a particular atomic configuration, with concomitant modification to Eq. (8) and the transition potentials therein. An energy spectroscopic diffraction pattern calculated in this way is shown in Fig. 6(b). The functions $\psi_{0,j}(\mathbf{R}, \mathbf{r}, z_i)$ are “auxiliary functions” since they no longer directly represent elastic scattering, as they do for that particular configuration in the frozen phonon model. In fact it is their coherent average which yields the wave function describing elastic scattering [73]. Since the transition potentials for ionisation tend to extend over a notably larger range than the length scale of atomic thermal motion, we note that a possible approximation is to use transition potentials at the equilibrium positions and modify only the $\psi_{0,j}(\mathbf{R}, \mathbf{r}, z_i)$ for the different configurations. Unlike in the frozen phonon model, we understand how to calculate the signals arising from elastically and thermally scattered electrons separately. This can afford important physical insights, as we will see shortly.

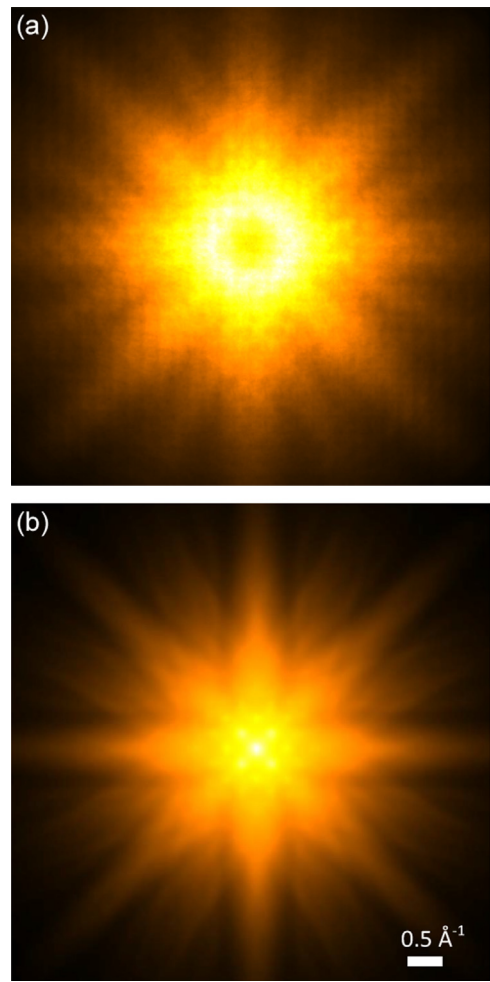


Fig. 6. (a) Contribution from thermally scattered electrons in the diffraction plane for scattering of 100 keV electrons from a 60 Å thick SrTiO₃ specimen formed with a convergent probe of aperture semi-angle 41 mrad positioned over a Sr column and displayed on a log scale. (b) Simulation of an energy-spectroscopic diffraction pattern for electrons that have ionised an oxygen K-shell electron for plane-wave illumination in SrTiO₃. The energy filter is set at 1 eV above threshold. The sample was 200 Å thick.

It is important to note the conceptual difference between the synthesis of the frozen phonon model and ionisation on the one hand and the incorporation of ionisation in the quantum excitation of phonons model. In the former, the total ionisation cross section is built up by *different* electrons, each scattering elastically off a *different* lattice configuration and then effecting ionisation. In the latter case we are predicting the ionisation cross section for a *single* electron scattering off the specimen elastically and possibly also thermally with ionisation possible at any stage. Inelastic scattering is treated in a quantum mechanical setting.

The similarity in the underlying physics for EDX and EELS mapping, alluded to earlier in this section, is borne out by the apparently anomalous behaviour sometimes seen in both EELS and EDX elemental maps for the oxygen K-shell signal in $\langle 001 \rangle$ strontium titanate: substantially more signal is obtained when the scanning probe is above columns containing both titanium and oxygen when compared with those containing only oxygen, despite the density of oxygen in both types of columns being the same (one atom per 3.905 \AA) [76]. Precisely this effect has also been noted in previous work by Dudeck and coworkers [77].

This conundrum can be understood using the quantum excitation of phonons model. This model allows one to track the contribution to the measured signal from both elastically and thermally scattered electrons separately. Considering thermal diffuse scattering, which is expected to redistribute the electron flux away from the column, one might initially argue that, for both the EELS and EDX cases, a lower signal should be obtained when the probe is on the Ti/O columns than when it is on the O columns. This view seems reasonable on the basis of previously reported EELS elemental maps, where it was seen that thermal diffuse scattering can reduce the signal from a column relative to off-column probe positions, explained by the depletion of the elastically scattered probe on the column by thermal scattering [9,78]. However, it is the contribution to the signal from thermally scattered electrons (those which have already excited a phonon, perhaps multiple times) that is key to understanding the enhancement of the O K-shell signal seen in the experimental data when the probe is on the column containing the heavier Ti atoms. Fig. 7 shows the simulated contribution to the signal for conditions similar to those reported in Ref. [76]. Considering only the contribution to the elemental map from elastically scattered electrons, the signal on the Ti/O column is somewhat less than on the pure oxygen columns, as seen in Fig. 7(b). However, the contribution on the Ti/O column from thermally scattered electrons is substantially more than when the probe is on pure oxygen columns, as seen in Fig. 7(b). Electrons are scattered away from the heavier Ti/O column (both elastically and thermally) and illuminate surrounding oxygen atoms, as shown in Fig. 8, which are ionised [76]. It is interesting to note that a similar effect is observed when the probe is on the Sr columns, which contain no oxygen atoms, as indicated by the peaks in the corners of Fig. 7(b).

5. Software to model imaging based on inelastic scattering

Software has been developed to simulate inelastic scattering using some of the ideas outlined in this paper and applications made by several authors. The book by Kirkland [64] can be consulted for details of simulations using the frozen phonon model and a small selection of other relevant papers are Refs. [41,79,80,20,81].

As already pointed out, propagators in 4D are numerically intensive, both in terms of memory requirements and in terms of processing power. Propagating the inelastic wave functions in 2D rather than density matrices in 4D makes the numerical calculations tractable. We are treating each transit of an electron through the specimen coherently. As per Eq. (14), each individual inelastic wave function

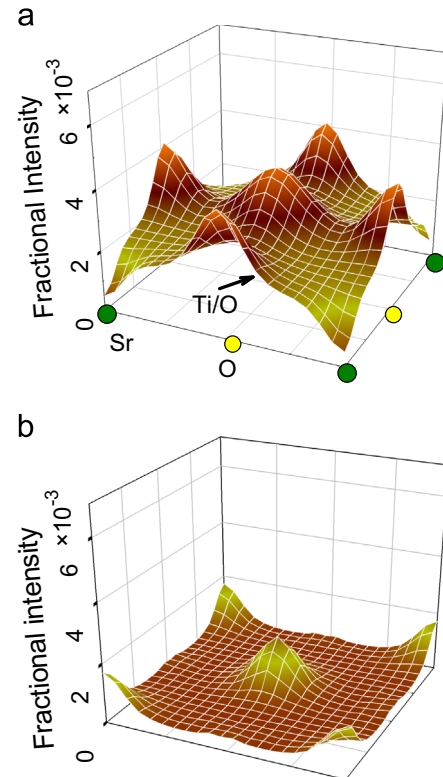


Fig. 7. Simulated contributions to an EDX elemental map using the signal in the oxygen K edge in $\langle 001 \rangle$ strontium titanate across a unit cell (a) due to ionisation by elastically scattered electrons and (b) due to ionisation by thermally scattered electrons. The projected structure is indicated: Sr columns green circles, visible O columns yellow circles and the arrow indicates the position of the Ti/O column. Parameters used: accelerating voltage 200 kV, probe-forming convergence semi-angle 23 mrad and specimen thickness 700 \AA . (For interpretation of the references to color in this figure caption, the reader is referred to the web version of this article.)

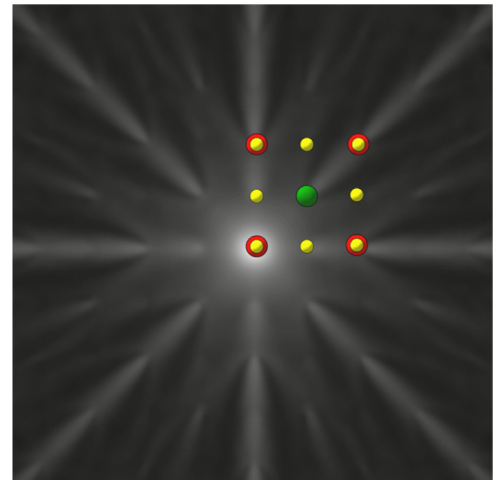


Fig. 8. Depth-integrated *real-space* distribution of thermally scattered electrons for a thickness of 700 \AA with the probe positioned over a Ti/O column in $\langle 001 \rangle$ strontium titanate. The specimen structure is overlaid. A logarithmic transformation $x \rightarrow \log(1 + Cx)$, where x is the pixel value and $C = 10^4$, has been applied to the calculated results to highlight interesting features. Parameters used are the same as those noted in Fig. 7.

has a well-defined phase, relating to both the phase of the elastic wave function in the plane of the transition and the transition potential, and as such it also scatters coherently. We then add the contribution in the diffraction plane from all possible final states incoherently. This is the

approach which has effectively been adopted in Refs. [20,41] and subsequent work based on these publications.

Here we will describe a software package which has mainly been developed at the University of Melbourne, but some of its underpinnings are from earlier Bloch wave code which was largely developed by Chris Rossouw. Historically, the package was developed with an emphasis on imaging in scanning transmission electron microscopy (STEM) and for that reason is dubbed μ STEM. To date version 1.0, which simulates elastic and thermal scattering in the quantum excitation of phonons model, has been released for download [82]. The code is also capable of simulations in the so-called absorptive model described early in Section 3. Similar calculations can also be carried out for conventional transmission electron microscopy.

Concurrent with the publication of this paper, version 2.0 of μ STEM is being released. This version is capable of modelling elemental mapping using EELS and EDX analysis based on inner-shell ionisation. In μ STEM it is assumed that the EELS detector covers the whole solid angle, because this makes it possible to compactly parametrise

scattering factors for a wide range of pertinent inner-shell ionisation edges as a function of the magnitude of the momentum transfer and energy loss, so that the local potential in Eq. (18) can be rapidly calculated. However, for large but finite detectors, even those with collection angles two to three times larger than the probe-forming aperture semi-angle, there can be considerable (mostly thermal) scattering outside of the detector of the probe electrons subsequent to causing ionisation events. This produces a discrepancy between the experiment, in which electrons scattered outside the detector do not contribute to the measured signal, and the simulations, in which the assumption of a detector spanning the whole solid angle includes the contribution from such electrons. Zhu et al. [83] recently proposed correcting experimental images for this sort of discrepancy by dividing the experimental maps by a normalised “incoherent bright field” image, the image formed with the same detector collection angle as the EELS image but integrated over the full energy range, elastic and thermal scattering included. We note that an alternative approach is to multiply the simulated EELS map, assuming a detector covering the whole solid angle, by a simulated incoherent bright field image

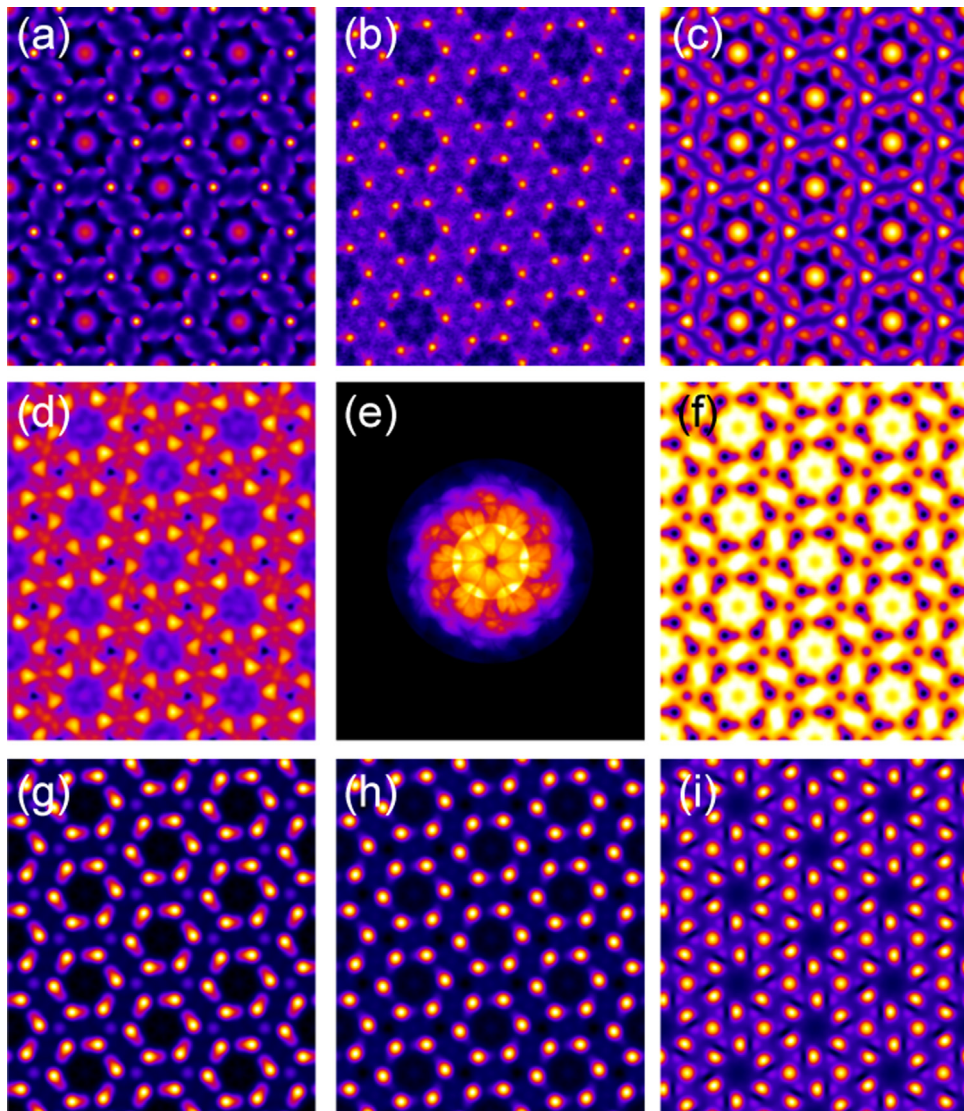


Fig. 9. Images calculated using μ STEM, as described in the text, using 100 keV electrons on a 300 Å thick specimen of [0001] Si_3N_4 . (a) Exit surface intensity due to elastically scattered electrons and (b) exit surface intensity due to thermally scattered electrons for plane wave illumination. In (c) and (d) the intensities in parts (a) and (b) after imaging by an aberration free lens with an aperture of 25 mrad are shown. (e) A position averaged convergent beam electron diffraction pattern calculated using an aberration-free, coherent probe formed using an aperture of 9.6 mrad with the average taken over the unit cell. (f) The annular bright-field image and (g) a high-angle annular dark-field image, using a probe formed using a 25 mrad aperture. Inner and outer angles are given in the text. An elemental map based on the energy-dispersive x-ray signal for the Si K edge is shown in (h) and for the N K edge in (i), using a probe forming aperture of 25 mrad. Each image is displayed on its own contrast scale.

assuming a detector with collection angle equal to that in the experiment (and expressed as a fraction of the incident intensity). In the quantum excitation of phonons model both elastic and thermally scattered electrons are included in the correction (other inelastic processes are a small contribution). In the absorptive model only elastically scattered electrons are included. The corrected map is also automatically generated by the code. This is an approximate approach. Exact calculations using the more general “nonlocal” formulation in Section 2 are of greater complexity and impose a substantial computational burden. Such calculations have been used when exploring subtle effects which arise when the acceptance angle of an energy-loss spectrometer is comparable to the angle of the aperture used to form a scanning probe, such as the “volcanos” shown in, for example, Refs. [84,85]. EDX maps are formed by integrating over all possible energies above the ionisation threshold and no correction is necessary for scattering outside a detector aperture, as in the case of EELS. This follows since the emission of x-rays, resulting from the filling of holes subsequent to ionisation events, occurs isotropically for all possible energy losses and kinematics. The x-ray signal is assumed to be proportional to the energy-loss signal calculated in this way – see for example Refs. [86] and references therein. Further details and information are in a manual [87], which, together with μ STEM 2.0, can be downloaded from the internet [82].

Fig. 9 shows a sample of the various imaging modes that can be simulated using μ STEM 2.0. We assume 100 keV electrons incident on a 300 Å thick specimen of Si₃N₄ down the [0001] zone axis. In Fig. 9(a) we show the intensity at the exit surface of electrons which have been elastically scattered in the specimen and in (b) the intensity of electrons that have been thermally scattered, both for plane wave illumination. Fig. 9(c) and (d) shows the intensities in parts (a) and (b) after the exit wave has been imaged by an aberration free lens with an aperture of 25 mrad. Fig. 9(e) is a position averaged convergent beam electron diffraction pattern formed using an aberration-free, focused coherent probe with a probe-forming aperture of 9.6 mrad (averaged over the unit cell). Fig. 9(f) shows an annular bright-field image (inner and outer angles 12.5 and 25 mrad) and Fig. 9(g) a high-angle annular dark-field image (inner and outer angles 60 and 160 mrad), once again for a probe formed using a 25 mrad aperture. An elemental map based on the energy-dispersive x-ray signal for the Si K edge is shown in Fig. 9(h) and on the N K edge in Fig. 9(i), once again using a probe forming aperture of 25 mrad.

6. Summary and conclusions

Starting with the early pioneering work of Harald Rose, we have reviewed progress in the imaging at atomic resolution based on the inelastic scattering of electrons over the last three decades, in particular the theoretical aspects. Applications to high-angle annular dark-field imaging and elemental mapping using electron energy loss spectroscopy or energy dispersive x-ray analysis have been discussed in some depth. The software package μ STEM 2.0, capable of simulating various imaging modes based on inelastic scattering in scanning transmission electron microscopy, and to a lesser extent in conventional transmission electron microscopy, has been introduced.

Acknowledgements

This research was supported under the Australian Research Councils Discovery Projects funding scheme (Projects DP110101570 and DP110102228) and its DECRA funding scheme (Project DE130100739). The authors acknowledge the important contribution of our collaborators and colleagues in the electron microscopy community to this

work. We would like to acknowledge the crucial contributions of Mark Oxley and Chris Rossouw to the theoretical and numerical aspects of the work discussed here. Eireann Cosgriff, Ben Forbes, Torgny Josefsson, Nathan Lugg, Andrew Martin, Gary Ruben and Chris Witte have been or still are members of the group at Melbourne University at various stages and all made contributions to the understanding of inelastic scattering discussed in this paper.

References

- [1] H. Kohl, H. Rose, Theory of image formation by inelastic scattered electrons in the electron microscope, *Adv. Electron. Electron Phys.* 65 (1985) 173–227.
- [2] N.D. Browning, M.F. Chisholm, S.J. Pennycook, Atomic-resolution chemical analysis using a scanning transmission electron microscope, *Nature* 366 (1993) 143–146.
- [3] N.D. Browning, M.F. Chisholm, S.J. Pennycook, Corrigendum, *Nature* 444 (2006) 235.
- [4] D.A. Muller, Y. Tsou, R. Raj, J. Silcox, Mapping sp² and sp³ states of carbon at sub-nanometre spatial resolution, *Nature* 366 (1993) 725–728.
- [5] P.E. Batson, Simultaneous STEM imaging and electron energy-loss spectroscopy with atomic-column sensitivity, *Nature* 366 (1993) 727–728.
- [6] K. Suenaga, M. Tencé, C. Mory, C. Colliex, H. Kato, T. Okazaki, H. Shinohara, K. Hirahara, S. Bandow, S. Iijima, Element-selective single atom imaging, *Science* 290 (2000) 2280–2282.
- [7] L.J. Allen, S.D. Findlay, A.R. Lupini, M.P. Oxley, S.J. Pennycook, Atomic-resolution electron energy loss spectroscopy imaging in aberration corrected scanning transmission electron microscopy, *Phys. Rev. Lett.* 91 (2003) 105503.
- [8] M. Varela, S.D. Findlay, A.R. Lupini, H.M. Christen, A.Y. Borisevich, N. Dellby, O.L. Krivanek, P.D. Nellist, M.P. Oxley, L.J. Allen, S.J. Pennycook, Spectroscopic imaging of single atoms within a bulk solid, *Phys. Rev. Lett.* 92 (2004) 095502.
- [9] M. Bosman, V.J. Keast, J.L. García-Muñoz, A.J. D’Alfonso, S.D. Findlay, L.J. Allen, Two-dimensional mapping of chemical information at atomic resolution, *Phys. Rev. Lett.* 99 (2007) 086102.
- [10] K. Kimoto, T. Asaka, T. Nagai, M. Saito, Y. Matsui, K. Ishizuka, Element-selective imaging of atomic columns in a crystal using STEM and EELS, *Nature* 450 (2007) 702–704.
- [11] D.A. Muller, L. Fitting Kourkoutis, M. Murfitt, J.H. Song, H.Y. Hwang, J. Silcox, N. Dellby, O.L. Krivanek, Atomic-scale chemical imaging of composition and bonding by aberration-corrected microscopy, *Science* 319 (2008) 1073–1076.
- [12] L.J. Allen, New directions for chemical maps, *Nat. Nanotechnol.* 3 (2008) 255–256.
- [13] O.L. Krivanek, N. Dellby, M.F. Murfitt, M.F. Chisholm, T.J. Pennycook, S. Kazutomo, N.V. Gentle STEM: ADF imaging and EELS at low primary energies, *Ultramicroscopy* 110 (2010) 935–945.
- [14] S. Trasobares, M. López-Haro, M. Kociak, K. March, F. de La Peña, J.A. Perez-Omil, J.J. Calvino, N.R. Lugg, A.J. D’Alfonso, L.J. Allen, C. Colliex, Chemical imaging at atomic resolution as a technique to refine the local structure of nanocrystals, *Angew. Chem. Int. Edition* 50 (2011) 868–872.
- [15] A.J. D’Alfonso, B. Freitag, D. Klenov, L.J. Allen, Atomic resolution chemical mapping using energy dispersive x-ray spectroscopy, *Phys. Rev. B* 81 (2010) 100101R.
- [16] M.W. Chu, S.C. Liou, C.P. Chang, F.S. Choa, C.H. Chen, Emergent chemical mapping at atomic-column resolution by energy-dispersive x-ray spectroscopy in an aberration-corrected electron microscope, *Phys. Rev. Lett.* 104 (2010) 196101.
- [17] L.J. Allen, A.J. D’Alfonso, B. Freitag, D.O. Klenov, Chemical mapping at atomic resolution using energy-dispersive x-ray spectroscopy, *MRS Bull.* 37 (2012) 47–52.
- [18] G. Kotheleitner, M.J. Neish, N.R. Lugg, S.D. Findlay, W. Grogger, F. Hofer, L.J. Allen, Quantitative elemental mapping at atomic resolution using x-ray spectroscopy, *Phys. Rev. Lett.* 112 (2014) 085501.
- [19] H. Rose, Image formation by inelastically scattered electrons in electron microscopy, *Optik* 45 (1976) 139–158.
- [20] L.J. Allen, S.D. Findlay, M.P. Oxley, C.J. Rossouw, Lattice-resolution contrast from a focused coherent electron probe. Part I, *Ultramicroscopy* 96 (2003) 47–63.
- [21] S.D. Findlay, L.J. Allen, M.P. Oxley, C.J. Rossouw, Lattice-resolution contrast from a focused coherent electron probe. Part II, *Ultramicroscopy* 96 (2003) 65.
- [22] H. Müller, H. Rose, P. Schorsch, A coherence function approach to image simulation, *J. Microsc.* 190 (1998) 73–88.
- [23] J. Verbeeck, D. Van Dyck, H. Lichte, P. Potapov, P. Schattschneider, Plasmon holographic experiments: theoretical framework, *Ultramicroscopy* 102 (2005) 239.
- [24] V.W. Maslen, C.J. Rossouw, The inelastic scattering matrix element and its application to electron energy loss spectroscopy, *Philos. Mag. A* 47 (1983) 119–130.
- [25] V.W. Maslen, C.J. Rossouw, Implications of (e,e)e scattering for inelastic electron diffraction in crystals. I. Theoretical, *Philos. Mag. A* 49 (1984) 735–742.
- [26] C.J. Rossouw, V.W. Maslen, Implications of (e,e)e scattering for inelastic electron diffraction in crystals. II. Application of the theory, *Philos. Mag. A* 49 (1984) 743–757.
- [27] D.K. Saldin, P. Rez, The theory of the excitation of atomic inner-shells in crystals by fast electrons, *Philos. Mag. B* 55 (1987) 481–489.

- [28] V.W. Maslen, On the role of inner-shell ionization in the scattering of fast electrons by crystals, *Philos. Mag. B* 55 (1987) 491–496.
- [29] D.K. Saldin, The theory of electron energy-loss near-edge structure, *Philos. Mag. B* 56 (1987) 515–525.
- [30] L.J. Allen, C.J. Rossouw, Effects of thermal diffuse scattering and surface tilt on diffraction and channeling of fast electrons in CdTe, *Phys. Rev. B* 39 (1989) 8313–8321.
- [31] L.J. Allen, C.J. Rossouw, Absorptive potentials due to ionization and thermal diffuse scattering by fast electrons in crystals, *Phys. Rev. B* 42 (1990) 11644–11654.
- [32] L.J. Allen, I.E. McCarthy, V.W. Maslen, C.J. Rossouw, Effects of diffraction on the (e,2e) reaction in crystals, *Aust. J. Phys.* 43 (1990) 453–464.
- [33] L.J. Allen, Electron energy loss spectroscopy in a crystalline environment using inner-shell ionization, *Ultramicroscopy* 48 (1993) 97–106.
- [34] L.J. Allen, C.J. Rossouw, Delocalization in electron-impact ionization in a crystalline environment, *Phys. Rev. B* 47 (1993) 2446–2452.
- [35] L.J. Allen, T.W. Josefsson, C.J. Rossouw, Interaction delocalization in characteristic X-ray emission from light elements, *Ultramicroscopy* 55 (1994) 258–267.
- [36] S.L. Dudarev, L.-M. Peng, M.J. Whelan, Correlations in space and time and dynamical diffraction of high-energy electrons by crystals, *Phys. Rev. B* 48 (1993) 13408–13429.
- [37] L.J. Allen, T.W. Josefsson, Inelastic scattering of fast electrons by crystals, *Phys. Rev. B* 52 (1995) 3184–3198.
- [38] P. Schattschneider, M. Nelhiebel, H. Souchay, B. Jouffrey, The physical significance of the mixed dynamic form factor, *Micron* 31 (2000) 333–345.
- [39] P. Schattschneider, W.S.M. Werner, Coherence in electron energy loss spectrometry, *J. Electron Spectrosc. Related Phenom.* 143 (2005) 81–95.
- [40] W. Coene, D. Van Dyck, Inelastic scattering of high-energy electrons in real space, *Ultramicroscopy* 33 (1990) 261–267.
- [41] C. Dwyer, Multislice theory of fast electron scattering incorporating atomic inner-shell ionization, *Ultramicroscopy* 104 (2005) 141–151.
- [42] K. Bluk, *Density Matrix Theory and Applications*, 3rd edition, Springer, Heidelberg, 2012.
- [43] S.D. Findlay, M.P. Oxley, L.J. Allen, Modeling atomic-resolution scanning transmission electron microscopy images, *Microsc. Microanal.* 14 (2006) 48–59.
- [44] A.P. Young, P. Rez, Resonance errors and partial coherence in the inelastic scattering of fast electrons by crystal excitations, *J. Phys. C: Solid State Phys.* 8 (1975) L1–L7.
- [45] N.R. Lugg, Atomic-resolution imaging using inelastically scattered electrons (Ph.D. thesis), The University of Melbourne, <http://repository.unimelb.edu.au/10187/14326>, December 2011.
- [46] S.L. Cundy, A. Howie, U. Valdre, Preservation of electron microscope image contrast after inelastic scattering, *Philos. Mag.* 20 (1969) 147.
- [47] N.R. Lugg, B. Freitag, S.D. Findlay, L.J. Allen, Energy-filtered transmission electron microscopy based on inner-shell ionization, *Ultramicroscopy* 110 (2010) 981–990.
- [48] K.W. Urban, J. Mayer, J.R. Jinschek, M.J. Neish, N.R. Lugg, L.J. Allen, Achromatic elemental mapping beyond the nanoscale in the transmission electron microscope, *Phys. Rev. Lett.* 110 (2013) 185507.
- [49] T.W. Josefsson, L.J. Allen, Diffraction and absorption of inelastically scattered electrons for K-shell ionization, *Phys. Rev. B* 53 (1996) 2277–2285.
- [50] C. Dwyer, S.D. Findlay, L.J. Allen, Multiple elastic scattering of core-loss electrons in atomic resolution imaging, *Phys. Rev. B* 77 (2008) 184107.
- [51] C. Dwyer, J. Etheridge, Scattering of Å-scale electron probes in silicon, *Ultramicroscopy* 96 (2003) 343–360.
- [52] D. Cherns, A. Howie, M.H. Jacobs, Characteristic X-ray production in thin crystals, *Zeitschrift für Naturforschung A* 28 (1973) 565–571.
- [53] K. Ishizuka, Prospects of atomic resolution imaging with an aberration-corrected STEM, *J. Electron Microsc.* 50 (2001) 291–305.
- [54] D.B. Williams, C.B. Carter, *Transmission Electron Microscopy*, Plenum Press, New York, 1996.
- [55] C.R. Hall, P.B. Hirsch, Effect of thermal diffuse scattering on propagation of high energy electrons through crystals, *Proc. R. Soc. Lond. Section A* 286 (1965) 158–177.
- [56] A. Howie, Image-contrast and localized signal selection techniques, *J. Microsc. Oxf.* 117 (1979) 11–23.
- [57] S.J. Pennycook, D.E. Jesson, High-resolution Z-contrast imaging of crystals, *Ultramicroscopy* 37 (1991) 14–38.
- [58] C.B. Boothroyd, R.E. Dunin-Borkowski, Contribution of phonon scattering to high-resolution images measured by off-axis holography, *Ultramicroscopy* 98 (2004) 115–133.
- [59] R.F. Loane, P. Xu, J. Silcox, Thermal vibrations in convergent-beam electron diffraction, *Acta Crystallogr. A* 47 (1991) 267–278.
- [60] D.A. Muller, B. Edwards, E.J. Kirkland, J. Silcox, Simulation of thermal diffuse scattering including a detailed phonon dispersion curve, *Ultramicroscopy* 86 (2001) 371–380.
- [61] D.M. Bird, Q.A. King, Absorptive form factors for high-energy electron diffraction, *Acta Crystallogr. A* 46 (1990) 202–208.
- [62] J.M. LeBeau, S.D. Findlay, L.J. Allen, S. Stemmer, Quantitative atomic resolution scanning transmission electron microscopy, *Phys. Rev. Lett.* 100 (2008) 206101.
- [63] R.F. Loane, P. Xu, J. Silcox, Incoherent imaging of zone axis crystals with ADF STEM, *Ultramicroscopy* 40 (1992) 121–138.
- [64] E.J. Kirkland, *Advanced Computing in Electron Microscopy*, Second edition, Springer, New York, 2010.
- [65] S.D. Findlay, M.P. Oxley, S.J. Pennycook, L.J. Allen, Modelling imaging based on core-loss spectroscopy in scanning transmission electron microscopy, *Ultramicroscopy* 104 (2005) 126–140.
- [66] H.L. Xin, C. Dwyer, D.A. Muller, Is there a Stobbs factor in atomic-resolution STEM-EELS mapping? *Ultramicroscopy* 139 (2014) 38–46.
- [67] C. Dinges, H. Rose, Simulation of transmission and scanning transmission electron microscopic images considering elastic and thermal diffuse scattering, *Scanning Microsc.* 11 (1997) 277–286.
- [68] J.S. Reid, Debye–Waller factors of zinc-blende-structure materials – a lattice dynamical comparison, *Acta Crystallogr. A* 39 (1983) 1–13.
- [69] H.X. Gao, L.M. Peng, Parameterization of the temperature dependence of Debye–Waller factors, *Acta Crystallogr. A* 55 (1999) 926–932.
- [70] Z.L. Wang, The ‘frozen-lattice’ approach for incoherent phonon excitation in electron scattering. How accurate is it? *Acta Crystallogr. A* 54 (1998) 460–467.
- [71] H. Yoshioka, Effect of inelastic waves on electron diffraction, *J. Phys. Soc. Jpn.* 12 (1957) 618–628.
- [72] D. Van Dyck, Is the frozen phonon model adequate to describe inelastic phonon scattering? *Ultramicroscopy* 109 (2009) 677–682.
- [73] B.D. Forbes, A.V. Martin, S.D. Findlay, A.J. D’Alfonso, L.J. Allen, Quantum mechanical model for phonon excitation in electron diffraction and imaging using a Born–Oppenheimer approximation, *Phys. Rev. B* 82 (2010) 104103.
- [74] C. Dwyer, Atomic-resolution core-level spectroscopy in the scanning transmission electron microscope, *Adv. Imaging Electron Phys.* 175 (2013) 145–199.
- [75] C. Dwyer, J.S. Barnard, Relativistic effects in core-loss electron diffraction, *Phys. Rev. B* 74 (2006) 064106.
- [76] B.D. Forbes, A.J. D’Alfonso, R.E.A. Williams, R. Srinivasan, H.L. Fraser, D.W. McComb, B. Freitag, D.O. Klenov, L.J. Allen, Contribution of thermally scattered electrons to atomic resolution elemental maps, *Phys. Rev. B* 86 (2012) 024108.
- [77] K.J. Dudeck, M. Couillard, S. Lazar, C. Dwyer, G.A. Botton, Quantitative statistical analysis, optimization and noise reduction of atomic resolved electron energy loss spectrum images, *Micron* 43 (2012) 57–67.
- [78] P. Wang, A.J. D’Alfonso, S.D. Findlay, L.J. Allen, A.L. Bleloch, Contrast reversal in atomic-resolution chemical mapping, *Phys. Rev. Lett.* 101 (2008) 236102.
- [79] C. Dwyer, Simulation of scanning transmission electron microscope images on desktop computers, *Ultramicroscopy* 110 (2010) 195–198.
- [80] S. Löffler, V. Motsch, P. Schattschneider, A pure state decomposition of the mixed dynamic form factor for mapping atomic orbitals, *Ultramicroscopy* 131 (2013) 39–45.
- [81] J. Verbeeck, P. Schattschneider, A. Rosenauer, Image simulation of high resolution energy filtered TEM images, *Ultramicroscopy* 109 (2009) 350–360.
- [82] muSTEM, <http://tcmp.ph.unimelb.edu.au/mustem/muSTEM.html>.
- [83] Y. Zhu, A. Soukiassian, D.G. Schlom, D.A. Muller, C. Dwyer, Towards artifact-free atomic-resolution elemental mapping with electron energy-loss spectroscopy, *Appl. Phys. Lett.* 103 (2013) 141908.
- [84] A.J. D’Alfonso, S.D. Findlay, M.P. Oxley, L.J. Allen, Volcano structure in atomic resolution core-loss images, *Ultramicroscopy* 108 (2008) 677–687.
- [85] M.P. Oxley, M. Varela, T.J. Pennycook, K. van Benthem, S.D. Findlay, A.J. D’Alfonso, L.J. Allen, S.J. Pennycook, Interpreting atomic-resolution spectroscopic images, *Phys. Rev. B* 76 (2007) 064303.
- [86] G. Kotleinikov, W. Grogger, M. Dienstleider, F. Hofer, Linking TEM analytical spectroscopies for an assumptionless compositional analysis, *Microsc. Microanal.* 20 (2014) 678–686.
- [87] A.J. D’Alfonso, μSTEM—Melbourne University Scanning Transmission Electron Microscopy computing suite, 2014.